Testing Emergent Bilateral Symmetry in Evolvable Robots with Vision

Michele Vannucci[1][a], Satchit Chatterji[2][b] and Babak H. Kargar[1][c]
[1]*Vrije Universiteit Amsterdam, The Netherlands*
[2]*University of Amsterdam, The Netherlands*
{*michele.vannucci20, babak.h.kargar*}*@gmail.com, satchit.chatterji@gmail.com*

Keywords: Evolution, Robotics, Symmetry.

Abstract: Bilateral symmetry is a prominent characteristic in the animal kingdom and is linked to evolutionary advantages such as cephalization. This study investigates whether integrating vision into modular evolvable robots influences bilateral symmetry development for a targeted locomotion task. Through simulation, we found that vision did not significantly increase our measure of symmetry in the robots, which predominantly evolved into 'snake-like' morphologies (with only one limb extending from the head). However, vision capability was observed to accelerate the convergence of the evolutionary process in some conditions. Our findings suggest that, while vision enhances evolutionary efficiency, it does not necessarily promote symmetrical morphology in modular robots. Further research directions are proposed to explore more complex environments and alternative symmetry measures.

1 INTRODUCTION

One of the most prominent features of terrestrial life is symmetry. Notably, a large swathe of life falls under the clade *Bilateria*, consisting of organisms that majorly exhibit bilateral symmetry. However, the origin and usefulness of such symmetry is highly debated within biology (Møller and Thornhill, 1998; Toxvaerd, 2021; Holló, 2015). It has been argued (e.g. in Finnerty, 2005) that bilateral symmetry is closely tied to the property of *cephalization*, that is, an organism having a distinct head and tail. Having a head with a concentration of perceptual organs (such as eyes, ears and a mouth) lends itself to improved self-perception of direction, as a front, back, left and right (also often up and down) can be defined with respect to the head. As a result, it was suggested by Finnerty (2005) that developing directionality along an axis of bilateral symmetry allows for better locomotion.

With respect to *perceptual* benefits as a result of cephalization, vision is an important one. In a number of contexts such as depth perception, low descriptional complexity and redundancy, bilateral symmetry provides a selection bias to animals with vision (Toxvaerd, 2021; Johnston et al., 2022). In contrast to this, there exist organisms with sight that are asymmetric (such as various species of flat fish) – however, their embryos are nevertheless symmetric, suggesting that they evolved from bilaterally symmetric ancestors to cover specific ecological niches (Friedman, 2008).

It is thus natural to ask to what extent (if at all) bilateral symmetry lead to the perceptual benefits offered by cephalization, and whether perception in turn influenced symmetry. Though this is difficult to test in the real world, it may be studied in simulated environments with a population of embodied organisms affected by evolutionary algorithms. Notably, the field of *evolutionary robotics* provides a framework where both the morphology (the 'body') and the control architecture (the 'brain') of each organism may be evolved simultaneously in a physical or simulated-physical environment (Eiben and Smith, 2015).

In this paper, we attempt to characterize the influence of directed vision in evolvable robots in a simulated environment with a targeted locomotion task in terms of the bilateral symmetry of their bodies. We hypothesize that the addition of vision capability will have a significant positive impact on the symmetry of the evolved robots.

2 BACKGROUND

To empirically assess our hypothesis we run the evolutionary process and physical simulations making

[a] https://orcid.org/0009-0008-1838-0562
[b] https://orcid.org/0009-0003-8648-1158
[c] https://orcid.org/0000-0003-4841-0597

Vannucci, M., Chatterji, S. and Kargar, B.
Testing Emergent Bilateral Symmetry in Evolvable Robots with Vision.
DOI: 10.5220/0012947400003837
In *Proceedings of the 16th International Joint Conference on Computational Intelligence (IJCCI 2024)*, pages 96-107
ISBN: 978-989-758-721-4; ISSN: 2184-3236
Copyright © 2024 by Paper published under CC license (CC BY-NC-ND 4.0)

use of Revolve2 (Computational Intelligence Group, 2023; Hupkes et al., 2018), a collection of Python packages used for researching evolutionary algorithms and modular robotics. We first briefly discuss about the robots themselves and some specifics about how they are generated. Next, we discuss the targeted locomotion task that the robots would evolve to optimize, and then the specifics of the evolutionary process utilized. Finally, we discuss how symmetry is currently defined in the context of modular robots.

2.1 Modular Evolvable Robots

Several studies have previously described modular robots in detail (e.g. the *Revolve* paper, Hupkes et al. 2018) and likewise evolvable morphologies and controllers (Miras et al., 2018, 2020a). Lan et al. (2021) provide a clear description of past studies in the field and experiments with a directed locomotion task.

In Lan et al. (2021) the controller is learned secondly to the recombination of the body, during a stage, namely ”infancy”, that precedes the ”mature” life, in which the phenotype is ultimately evaluated for selection. In contrast, in our experiment both the controller and the robot body are recombined at the same time. This happens through the HyperNEAT (Stanley et al., 2009) algorithm before each new generation, meaning that the robot doesn’t learn during the simulation, and is evaluated only one time at end of its life. This algorithm as been shown to work well on evolving modular robots controllers as far back as 2010 (Haasdijk et al., 2010).

Our robot has three types of modules: the core, active hinges and brick modules. Both the controller and the body genotypes are developed through a compositional pattern-producing network (CPPN), that is evolved with HyperNEAT as already mentioned. This method of separating the components of the robot genotype in two parts has been already covered in past research as in Jelisavcic et al. (2019) for which Figure 1 is illustrative.

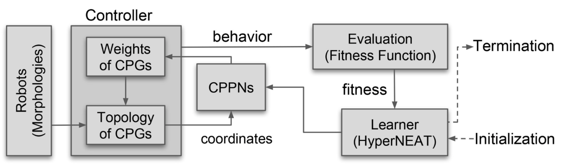

Figure 1: The complete architecture of the learning system. Image reprinted from Jelisavcic et al. (2019).

- **The body** is represented as a tree structure that starts from the core and new modules are recursively attached based on the orientation of the parent on the empty sides. The CPPN takes as input the position of the potential children modules defined in a three-dimensional grid space, and the length of the shortest path of the node to the core. The output is the node type, which can also be empty, terminating the branch, and how it should be oriented. This results in a three-dimensional robot.
- **The controller** phenotype is developed based on the underlying morphology of the robot, using a technique that has been proven working with modular robots on different kinds of tasks by past studies (De Carlo et al., 2020; Lan et al., 2021). The final controller is a central pattern generator network (CPG) which has, for each joint/hinge i, three neurons x_i, y_i (connected bidirectionally), and o_i, which has one in-going connection from x_i. The cyclical connection between the x and y neurons allow the periodical propagation of the signal, while the o neuron provides the output controlling the one degree of freedom joint with a value in the range $[-1.0, 1.0]$. To propagate to all parts of the robot information about the other joints all the x neurons have a bidirectional connection between each other with weights $w_{x_j x_i}$ and $w_{x_i x_j}$, where i and j are two different hinges. Figure 2 gives an example representative illustration. All the weights are learned and computed by the CPPN that takes as input a 8-dimensional vector, three dimensions each for the position of the first and second neuron respectively and one dimension each that encodes their type (x, y or o).

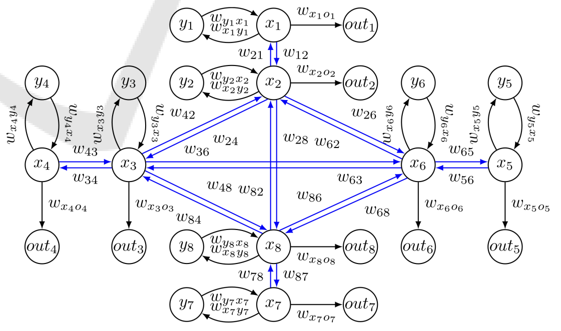
y_1 x_1 out_1
y_2 x_2 out_2
y_3 x_3 out_3
y_4 x_4 out_4
y_5 x_5 out_5
y_6 x_6 out_6
y_7 x_7 out_7
y_8 x_8 out_8
w_{21} w_{12} w_{42} w_{24} w_{43} w_{34} w_{36} w_{26} w_{28} w_{62} w_{48} w_{82} w_{84} w_{86} w_{63} w_{68} w_{65} w_{56} w_{78} w_{87}

Figure 2: Example CGP controller of a robot with 8 active hinges. Image reprinted from Lan et al. (2021).

2.2 Targeted Locomotion

The goal of any evolutionary algorithm across generations is the optimization of a function that individuals in a generation are evaluated against. In our experiment, we begin by placing the modular robot at the origin of a 3D environment and evaluate it based on how far it is to a predetermined target $\vec{t} = (x_t, y_t)$ on the ground at the end of the simulation (i.e. after a certain number of timesteps in simulated time). This target is the same for all individuals in the population of the same generation so they may be compared. The fitness function is set simply to the negative of the Euclidean distance from the final location of the core of the robot with respect to this target. Thus the algorithm aims to maximize the following function for the robots R with final core location $\vec{loc}_R = (x_R, y_R)$:

$$f(R) = -|\vec{loc}_R - \vec{t}| \quad (1)$$

$$= -\sqrt{(x_R - x_t)^2 - (y_R - y_t)^2} \quad (2)$$

Note that while the core of the robot technically has a 3D location (with a potentially non-zero height), the above equation simplifies this by using the projection of its position onto the xy-plane.

We also experimented using the squared distance, as it can provide higher evolutionary pressure in the first few generations, but we empirically concluded that this is helpful only in the first part of the evolution process, as it accelerates the improvement of the first generations but stagnates later – after around 100 generations the robots would reach the same fitness plateau as the ones evolved with the regular distance metric. Thus, for simplicity, we opted for Equation 1.

2.3 The Evolutionary Process

In this section, we describe techniques used for each phase of the evolutionary algorithm. This is a brief summary of a fairly common method, and we direct the readers to Eiben and Smith (2015) and Hupkes et al. (2018) for more thorough descriptions.

2.3.1 Initialization

The $\mu \in \mathbb{N}$ CPPN genotypes of the first generation are initialized as *empty*, after which the HyperNEAT mutation is applied 5 times to introduce initial diversity. In this phase the robots of the starting generation are also evaluated to assign them fitness values to kick-off the iterative evolution process.

2.3.2 Parent Selection

$\lambda \in \mathbb{N}$ pairs of parents are selected randomly over the μ members of the current generation. This allows the selection pressure to be localized only in the later survivor selection phase.

2.3.3 Mutation and Crossover

Mutation and crossover are run (in that order) over all the pairs of selected parents using the HyperNEAT algorithm already mentioned, and the specific hyperparameters used are detailed in Section 3.2. This phase creates λ offsprings.

2.3.4 Evaluation

In this phase λ simulations are run in parallel to evaluate the newly generated offsprings using the fitness function described in Equation 1. More specifics on the physics simulations will follow in Section 3.

2.3.5 Survivor Selection

In this phase we use $(\mu + \lambda)$ selection (Eiben and Smith, 2015, sec. 5.3.2), as we select μ robots from the union set of the current generation and the offsprings. In this phase, tournament selection is performed with k sampled individuals.

2.3.6 Termination Criteria

After each new generation is created, steps 2.3.2 to 2.3.5 are repeated. The termination criteria is set to a predetermined maximum number of generations $G_{\max}$.

2.4 Symmetry

Miras et al. (2020b) define an approximation of bilateral symmetry along two axes with respect to the the core of a 2D robot (Equation 3),

$$Z = \max(z_v, z_h) \quad (3)$$

The values z_v and z_h represent the symmetry values along the vertical (x) and horizontal (y) axes respectively when seen from a top-down view.

In our case, since the robot body develops itself in three-dimensional space, instead of calculating the symmetry with respect to one-dimensional axes, we do it with respect to the x-z and the y-z planes, which generalize the symmetry values defined above for a 3D robot placed on the x-y plane (i.e. parallel to the floor). Given that the position of the core of some robot is located at (x_c, y_c, z_c), the planes of symmetry to compute $z_{x\text{-}z}$ and $z_{y\text{-}z}$ are defined as $x = x_c$ and $y = y_c$ respectively. Finally the symmetries are calculated, with a score in the interval $[0, 1]$, ignoring the modules on the plane of symmetry (where the "spine" of the robot is) with an analogous equation to Equation 3:

$$Z_{3D} = \max(z_{x\text{-}z}, z_{y\text{-}z}) \quad (4)$$

Closely related to the method by Miras et al. (2020b), we count the number of connected modules on one side of each respective plane that has a mirrored module on the other side, and multiply this by two.

Finally, we divide this value by the total number of modules compared. The modules that lie on each respective plane are not considered in this computation as well.

3 METHODS

The code[1] was implemented in Python 3.10 making use of the already meantioned Mujoco-based library Revolve2 (Computational Intelligence Group, 2023) pre-release version v0.4.0-beta2. This was the base of our implementation, from the evolutionary algorithm to physics simulation of the modular robots. The fitness function used is Equation 1 as discussed previously, while the symmetry measure (Equation 4) was also collected at the end of each generation for every individual. Significant additional contributions with respect to our experiments are discussed below.

3.1 Vision-Augmented Steering

A fundamental aspect of our research is the addition of visual perception to the robot controller that, in its default implementation, does not possess a *vision* component. The latter is needed to implement what we refer to as the 'steering behavior' of the robot within this paper. To achieve this, we added a Mujoco camera in the environment with its position and orientation locked to that of the core (i.e. the robot always looks 'forward' with respect to its core).

To connect the camera input to the controller we adapted a technique introduced in Luo et al. (2022) that consists of directly altering the CPG output values based on a measure of the error angle θ between the target direction and the robot direction. In Luo et al. (2022) θ was calculated directly using the coordinates of the target and the robot. However, in our case, it is done creating a mask onto the camera image to detect the red sphere object that represents the target. This is done with a boolean condition on every pixel of an input frame, defined as $M_{x,y} = (G_{x,y} < 100) \wedge (R_{x,y} > 100) \wedge (B_{x,y} < 100)$, where $G_{x,y}$, $R_{x,y}$ and $B_{x,y}$ are the intensity values of the green, red and blue RGB channels respectively for the pixel positioned at coordinate (x,y) (the origin is placed at the top left of the image). Subsequently, we compute the mean x and y values for pixels where the condition is satisfied to get the position (x_s, y_s) of the center of the portion of the sphere in the camera frame. θ and g are then calculated as:

[1]The code can be found at https://github.com/satchitchatterji/OriginOfSymmetry

$$\theta = \frac{w_{cam}}{2} - x_s \quad (5) \qquad g(\theta) = \frac{\frac{w_{cam}}{2} - |\theta|^n}{\frac{w_{cam}}{2}} \quad (6)$$

Where w_{cam} is the width of the camera image in pixels and n is a parameter that we set to 7 (value taken from Luo et al., 2022). Since θ is a value in the range $[0, \frac{w_{cam}}{2}]$, g will be in the range $[0, 1]$. Finally, g is directly applied as a factor to the output o_i of the neuron for joint i, depending on where the joint of the robot is with respect to its core. If the joint is on the left side of the body, it uses the formula:

$$o_i = \begin{cases} g(\theta) \cdot o_i & \text{if } \theta < 0 \\ o_i & \text{if } \theta \geq 0 \end{cases}$$

Thus, it is slowed down when the target is on the right side of the robot's visual field ($\theta < 0$). Analogously, if i is on the right hand-side of the robot the following formula is applied:

$$o_i = \begin{cases} o_i & \text{if } \theta < 0 \\ g(\theta) \cdot o_i & \text{if } \theta \geq 0 \end{cases}$$

This method doesn't necessarily benefit every possible robot, but it is expected that the ones that take advantage of it would emerge through selection.

3.2 Hyperparameter Selection

Table 1: Hyperparameter selection for targeted locomotion task. The "Selection Set" refers to the list of hyperparameter options tested for that variable. The variables selected for the full experiment are in bold.

Hyperparameter	**Selection Set**
Population size (μ)	$\{\mathbf{100}\}$
Offspring size (λ)	$\{\mathbf{50}\}$
Num. of generations ($G_{\max}$)	$\{50, 100, \mathbf{200}\}$
Brain mutation rate (p_{brain})	$\{0.9, \mathbf{0.15}, 0.2\}$
Body mutation rate (p_{body})	$\{0.9, \mathbf{0.15}, 0.2\}$
Tournament size (k)	$\{3, \mathbf{6}\}$

Firstly, population size and offsprings size (μ and λ) were fixed to 100 and 50 respectively, as they are reasonable amounts that have already been proven working for similar tasks (for example, Luo et al., 2022). We also trialed higher numbers, but the improvements in fitness weren't significant enough to justify the increase in computation time.

Secondly, the number of generations G_{max} was set to 200 to assure that the convergence was reached before the end of the experiment as we saw in pilot experiments that this would happen around the 100th generation for a population size of 100.

Subsequently, the final parameters that we selected were the HyperNEAT mutation values and the tournament size k. Since our HyperNEAT implementation has over 30 parameters we focused only on the overall mutation rate for “brain” and “body” separately (p_{body} and p_{brain}), while keeping the remaining values as those that can be found in the default Revolve implementation. Finally, p_{body}, p_{brain} and k were selected simultaneously through grid search, considering both scenarios where the camera functionality was activated or deactivated. More details on this sweep can be found in Appendix A. All the hyperparameters we opted for can be found in Table 1.

3.3 Experimental Conditions

All robots are initially placed at coordinate $(0,0,0)$. Three target conditions were selected for the final experiment, each placed at $z = 1$:

- The first condition, T_1, is where the target for all individuals was placed at the coordinate $(5,5)$, i.e. in front and to the right of the robot.
- In the second condition, T_2, the target was placed at the coordinate $(0,\sqrt{50})$, right in front of the robot and at the same distance as in T_1 to ensure just comparisons between conditions.
- Finally, the third condition, T_3, consisted of cyclically changing the target in after each generation from (*i*) the left of the robot, $(-5,5)$, (*ii*) straight ahead, $(0,\sqrt{50})$, and (*iii*) to the right $(5,5)$. Generation 0 had the same target as generation 3 (to the left); generation 1 had the same as generation 4 (in front); generation 2 had the same as generation 5 (to the right), and so on. All robots in a single generation were tasked with reaching the same target. Therefore, under this condition, the robot should be able to reach the target regardless of its location to optimize fitness.

Each condition has two sub-conditions, the case where the robot has vision and the one where it doesn’t. Each condition was tested at least 10 times in total (5 times per sub-condition).

4 RESULTS

The code was run on a Mac Pro with an M2 chipset. A single generation with steering took about 30 seconds with a population size of 100. No-steer runs took about 20 seconds with the same configuration.

In the remainder of this section, we present aggregated results concerning the training (Section 4.1) and behaviors exhibited (Section 4.2) by the evolved robots, exploring how those may affect the primary hypothesis that vision influences symmetry (Section 4.3). We also present an additional post hoc result about the speed of convergence of the evolutionary algorithm in this task (Section 4.4). For completeness, we present graphs which aggregate the maximum fitnesses and symmetries per generation in Appendix C, though for our analysis, Figure 4 suffices (portraying the means of the same).

4.1 Fitness

To test our hypothesis properly we first needed the robots to reach the target consistently. This was enabled by the hyperparameter tuning process detailed in Section 3.2. In the the left column of Figure 4 we compare how the two types of robot, with vision and without, perform across the generations for all three conditions in order for the main experiments.

We can see that for conditions T_2 ad T_3 (Figures 4c and 4e) the robots with steering functionality converge to an optimal fitness (around zero) faster than those without across multiple experiments. We discuss this further in Section 4.4.

This trend isn’t that clear for condition T_1 (Figure 4a), but still holds when we aggregate all three conditions together. This can be explained by the fact that for T_2, the optimal final position is $(0,\sqrt{50})$, while for T_3 the one that leads, on average, to best the fitness, is located on the Fermat point (Weisstein, 2003) of the triangle generated by the three targets, which is $(0,\sqrt{50})$. This means that, for both conditions, the robot needs to go straight, which is easier. We didn’t expect this behavior – the robots, even with vision, get stuck on the local optima. This is illustrated in the next section.

4.2 Paths

Since the fitness trend and manually looking at the videos from the robot’s perspective wasn’t sufficient to have a clear overview of the robots’ behavior inside the simulation, we generated graphs displaying the paths taken by a sample of robots within the same generation. In Figures 3a and 3b we can see how they evolve between generation 50 and 150 for condition T_1, while in Figures 3c and 3d we have the same comparison for condition T_3.

Under condition T_1 the robots improve their fitness by moving straight ahead, further on at generation 150 they appear to have learned how to navigate to the target on the right, displayed with a green cross. On the other hand, for condition T_3 the robots, en-

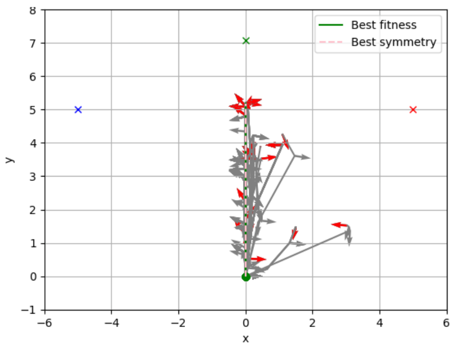

(a) Condition T_1, generation 50

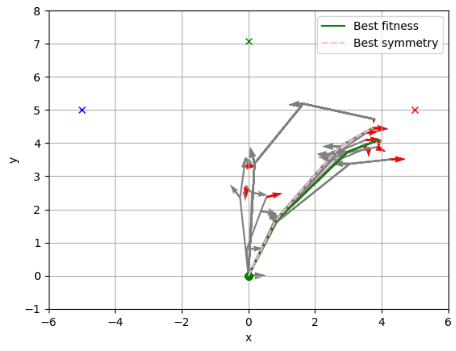

(b) Condition T_1, generation 150

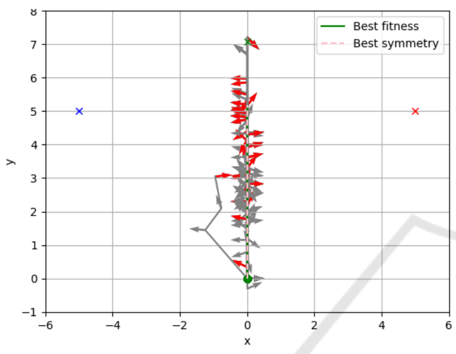

(c) Condition T_3, generation 50

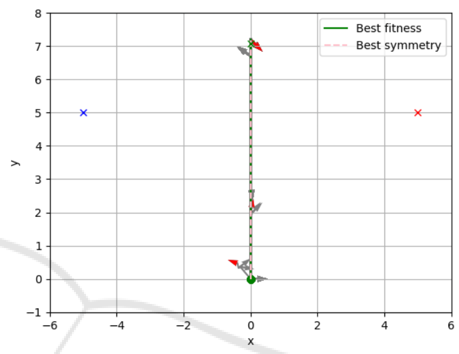

(d) Condition T_3, generation 150

Figure 3: Example paths (grey lines) without steering functionality. For T_1 (top), the target is shown by the red cross. For T_3, (bottom) the 3 cyclically changing target are shown as red, blue and green crosses respectively. Condition T_2 (with the target being the green cross) shows similar paths to T_3 and is excluded here for the sake of brevity. Grey arrows represent the intermediary 2D orientations of the robot's core, and red arrows show the final orientations. The green path shows one of the robots with the best fitness, and the dotted orange line is the path of one of the robots with the best fitness (there may be multiple individuals with the same fitness and/or symmetry in one generation).

SCITEPRESS SCIENCE AND TECHNOLOGY PUBLICATIONS

dowed with vision capability, seem to reach the Fermat point quickly as already at generation 50 they are in its close vicinity, we observed a similar behavior for robots without vision. We can't say confidently that the robots are taking advantage of the camera to move towards the target. Looking at the paths we can confirm that, even when provided with the steering behavior, they merely go towards the Fermat point. Nevertheless, this doesn't explain why the plots of the mean fitness *don't* have steeper dips, as the targets $(-5,5)$ and $(5,5)$ are more than 5 units away from the Fermat point, while the mean fitness decreases only by ≈ 0.5. We are unsure of why this happens.

4.3 Main Result: Symmetry & Vision

Looking at the graphs for condition T_2 and T_3 (Figures 4d and 4f), it is evident that, according to our measure of symmetry, as the robots adapt and their fitness values increase, the symmetry shrinks to 0. This is slightly different for condition T_1 (Figure 4b) for which there is no rapid convergence trend as some experiments did not produce a robot capable of reaching the target.

As shown in the right column of Figure 4, we see that the experiments dependably create robots that are *not* symmetric with or without vision. We compare the mean of the symmetries of the generations over all the runs for each experimental condition for the steer and no-steer robots using a Mann-Whitney U test. This results in $p >> 0.05$, even approaching $p = 1$ for T_2 and T_3. This test was used as the assumptions of the standard t-test cannot be verified (notably, the normality test and the low sample size). Furthermore, the symmetry values themselves approach zero (testing the hypothesis that the symmetries are non-zero results in $p \to 1$ as generations increase for T_2 and T_3). Thus, we fail to reject our null hypothesis that robots with vision evolve to be more symmetric than those without.

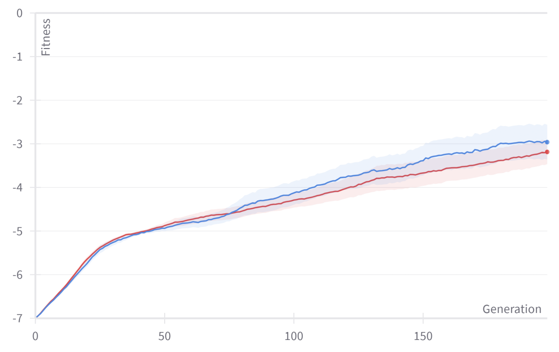

(a) Fitness results for condition T_1.

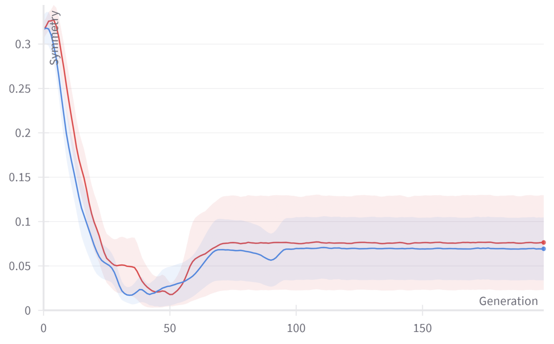

(b) Symmetry results for condition T_1

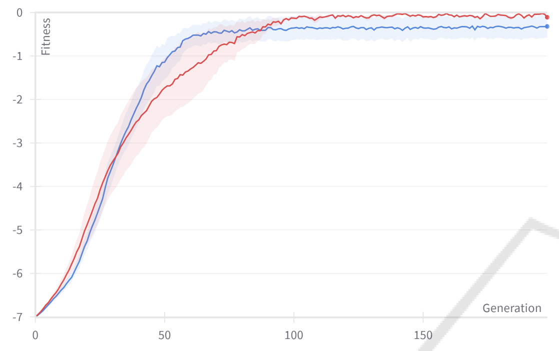

(c) Fitness results for condition T_2.

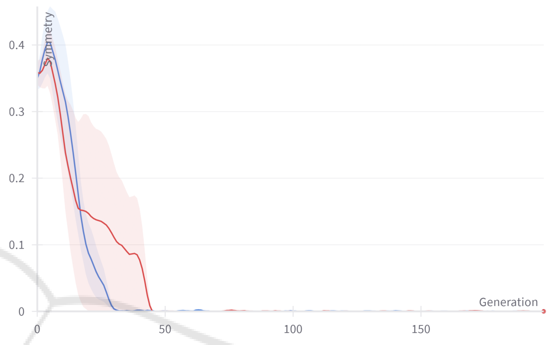

(d) Symmetry results for condition T_2

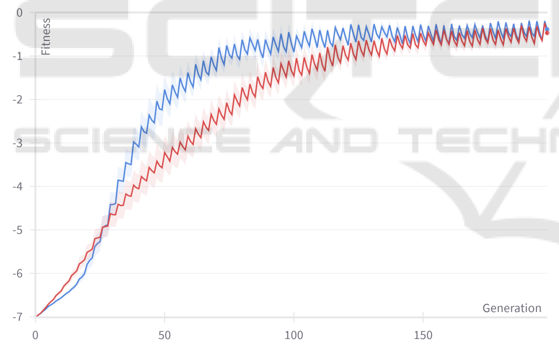

(e) Fitness results for condition T_3.

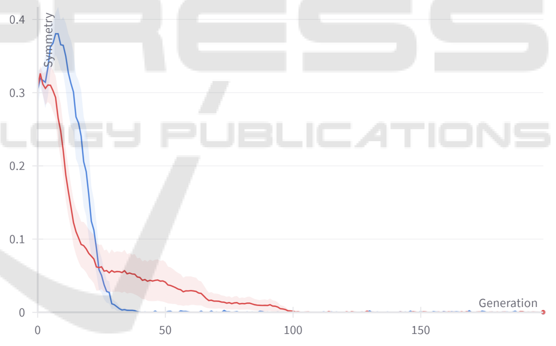

(f) Symmetry results for condition T_3

SCITEPRESS
SCIENCE AND TECHNOLOGY PUBLICATIONS

Figure 4: Mean of (mean fitnesses per generations, left) and mean of (mean symmetries per generations, right) over all runs for robots with steering behavior (blue) and without (red). The x-axis is the generation index and the y-axis is the fitness according to Equation 1 (left) or 3D symmetry according to Equation 4 (right). The shadows represent standard error.

4.4 Additional Result: Rate of Convergence

Finally, we demonstrate the improvement of convergence for robots augmented with vision. Since we could not find a standard way to quantify the speed of convergence, we first aggregated each population to a mean fitness value, then grouped all experiments according to whether the robots had steering or not. We then applied a Mann-Whitney U test to see whether having vision significantly makes a difference in the fitness means across generations. This test was used as the assumptions of the standard t-test could not be justified. The results can be seen in Figure 5. We note significant differences ($p << 0.05$) in a large portion of generations in condition T_3 from generation 30 to around generation 130 (with the lowest $p \approx 0.0002$). Looking at the training graph in Figure 4e, we see that the convergence graphs between the steer and no-steer conditions deviate significantly between these generations, meaning the robots that have vision converge to a solution with the same fitness as those that don't, but faster.

For condition T_2, although we can visually see faster convergence for robots with vision, this is not reflected in the Mann-Whitney U tests: the p-value approaches $p = 0.05$ but never crosses it, and thus there is no significant difference for any generation.

Lastly, the p-values for T_1 are relatively large, (the lowest p-value ≈ 0.155), and thus the convergence rates are not significantly different at all.

5 DISCUSSION

This paper demonstrates first steps in attempting to verify if vision may affect symmetry in evolvable modular robots. Although we did not find significant results, it must be recognized that this paper is a small slice of possible experiments in this vast area. Here, we reflect on various aspects of this paper and directions in which future research may venture.

5.1 Robot Morphology and Symmetry

After failing to reject our initial null hypothesis about the effect of vision on symmetry (Section 4.3), we dug deeper to find out what kinds of robots the experiments were actually producing. When examining the bodies of the robots, we noticed an interesting trend. The morphologies of the robots all tended towards a core with a long line of active hinges, as seen in Figure 6. We offer a straightforward explanation for this phenomenon, derived from observing simulation videos. The evolutionary algorithm determined that this was the most efficient anatomy as it enabled the robots to execute one or more large jumps, propelling them towards the target more rapidly. This is also confirmed by the path plots (Figure 3) which illustrate the robots' seemingly random orientations during intermediate states as they rotate while jumping. In Section 5.2 we suggest how this could be avoided using a different fitness function. These findings, in addition to Equation 4, explain why the symmetries of the evolved robot population (in the right column of Figure 4) tended to go to zero.

In a sense we can argue that the evolved robots *are* symmetrical, perhaps trivially so (as, for example, a worm is considered bilaterally symmetric in biological literature). Thus, it is possible that the current definition of symmetry as per Miras et al. (2020b) and Equation 4 is either insufficient or inadequate to be used when comparing evolvable robots to real evolution. An alternative may be to take all modules into account when computing symmetry (instead of ignoring those that lie on the plane of symmetry) or to use an alternative measure such as the symmetry of the planar images of the robots. Additionally, there exist animals in nature with other forms of symmetry (notably rotational symmetry), and thus an analogue may be useful in the context of evolvable robotics too.

5.2 Further Developments

In conclusion, as already suggested, a number of aspects of this research could be developed further for future studies, a selection of possible improvements include:

- **More Detailed Hyperparameter Selection:** A large majority of our hyperparameters were chosen based on other papers (notably Miras et al., 2018 and Luo et al., 2022) that have been shown to work in tasks similar to ours. However, with the additonal element of vision, the optimal hyperparameters may not be the same as theirs. Though we did do some tuning, a fuller search (requiring substantial compute) may be needed to explore this topic fully.
- **More Efficient Computation:** One of the challenges faced during this project was the fact that running the experiments was often time-consuming and not cross-platform. Thus, for a more complete experiment (especially those that aim to do a fuller hyperparameter selection sweep), we suggest finding ways to make this computation faster and more robust. We attempted to work towards this by heuristically minimizing the simulation time of the environment for each robot, and though it showed promising results, we did not have time to fully flesh this out. A description of this can be found in Appendix B.
- **Fitness Function:** The fitness function defined previously (Equation 1) was kept simple in order not to have too many confounding variables in our analysis. Thus, the simplest fitness for a targeted locomotion task is the Euclidean distance between the target and the final robot position. However, future studies may augment this to include other aspects of movement, such the length and shape of the full path to the target or the orientation of the robot's core, as was done in Luo et al. (2022). This could force the robots to reach the target through a more rectilinear and natural locomotion. That, in turn, could lead to more bilateral morphologies that differ from those described in Section 5.1.
- **Symmetry:** As discussed earlier, the symmetry measure adapted from Miras et al. (2020b) may

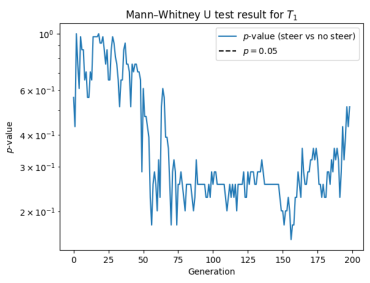

(a) Results for condition T_1.

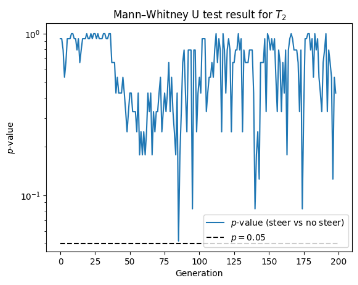

(b) Results for condition T_2

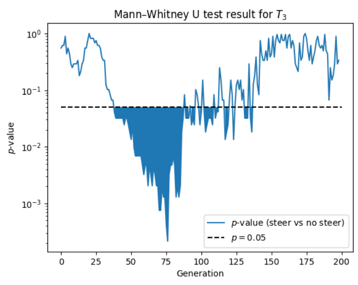

(c) Results for condition T_3

Figure 5: Mann-Whitney U test across each generation to compare the means of fitnesses for robots with steering vs no steering behaviour. The y-axis is log-scaled for clarity, and the dotted line represents the standard significance level of $p = 0.05$. Note that in the T_2 condition, the significance reference line is too low to be displayed. The shaded area represents the portion of the graph that lies under $p = 0.05$. Refer to Section 4.4 for details.

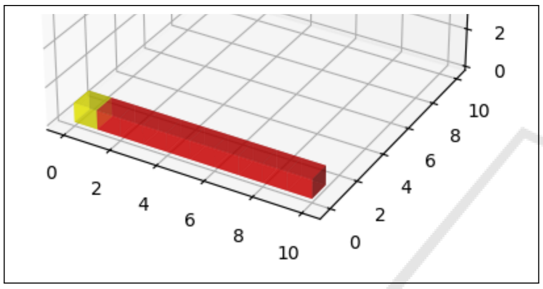

Figure 6: Most common robot morphology evolved at convergence in all experiments. Each 1×1 box is a single module: the yellow voxel represent the core, and the red voxels represent active hinge modules.

not cover all aspects of visual and biological symmetry. Thus, a variety of alternatives may need to be developed to verify their usefulness and to allow a fairer comparison with biological organisms. Additionally, nature shows other pattern types such as fractals, which may be interesting to study in the context of larger evolvable robots.

- **Other Morphological Measures:** In addition to symmetry, other morphological measures may be interesting to study as vision is incorporated, for example, balance, or the number of limbs. Kargar et al. (2021) and Miras et al. (2018) list a number of measures in this direction.
- **Vision Implementation:** Our implementation of vision follows Luo et al. (2022), as the target information extracted from the video is used directly to influence the outputs for the joints in the controller network. Though this worked for their needs, it does introduce bias for the simplicity of the model and a new hyperparameter (with respect to Equation 6). Thus, given enough computing resources, it may be more natural for a system to evolve end-to-end, i.e. the camera feed is used as an *input* to the controller network, with which it may gain useful information about its environment. For example, depending on the task, this may be in the form of a bag-of-words histogram or even a convolutional neural network (being careful of its inductive bias of translational invariance) that is pre-trained or co-evolved with the robot's brain and body.
- **More Complex Tasks/Environments:** The task of targeted locomotion is fairly simple, and was chosen indeed for its simplicity. However, this may have been the cause of the rejection of the null hypothesis in this paper – perhaps the environment was *too* simple for there to be a significant advantage of having vision and of developing symmetry. A different task (such as survival or balance), or more complex environments (elements of non-stationarity or partially-observable states) may lead to a fairer test of the hypothesis.
- **Studying the Effect of Vision on Convergence:** Although we cannot gather much evidenced for the effect of vision on symmetry, we uncovered an interesting trend in Section 4.4 that robots with vision *may converge quicker* than those without. Thus, using this work as a jumping off point, it may be beneficial for future research to study this in more detail, and verify which tasks and environments also produce this trend.

REFERENCES

Computational Intelligence Group, V. U. A. (2023). Revolve2. https://github.com/ci-group/revolve2. Version used: 0.4.2.

De Carlo, M., Zeeuwe, D., Ferrante, E., Meynen, G., Ellers, J., and Eiben, A. (2020). Robotic task affects the resulting morphology and behaviour in evolutionary robotics. In *2020 IEEE symposium series on computational intelligence (SSCI)*, pages 2125–2131. IEEE.

Eiben, A. E. and Smith, J. E. (2015). *Introduction to evolutionary computing*. Springer.

Finnerty, J. R. (2005). Did internal transport, rather than directed locomotion, favor the evolution of bilateral symmetry in animals? *BioEssays*, 27(11):1174–1180.

Friedman, M. (2008). The evolutionary origin of flatfish asymmetry. *Nature*, 454(7201):209–212.

Haasdijk, E., Rusu, A. A., and Eiben, A. E. (2010). Hyperneat for locomotion control in modular robots. In *Evolvable Systems: From Biology to Hardware: 9th International Conference, ICES 2010, York, UK, September 6-8, 2010. Proceedings 9*, pages 169–180. Springer.

Holló, G. (2015). A new paradigm for animal symmetry. *Interface focus*, 5(6):20150032.

Hupkes, E., Jelisavcic, M., and Eiben, A. E. (2018). Revolve: a versatile simulator for online robot evolution. In *Applications of Evolutionary Computation: 21st International Conference, EvoApplications 2018, Parma, Italy, April 4-6, 2018, Proceedings 21*, pages 687–702. Springer.

Jelisavcic, M., Glette, K., Haasdijk, E., and Eiben, A. (2019). Lamarckian evolution of simulated modular robots. *Frontiers in Robotics and AI*, 6:9.

Johnston, I. G., Dingle, K., Greenbury, S. F., Camargo, C. Q., Doye, J. P., Ahnert, S. E., and Louis, A. A. (2022). Symmetry and simplicity spontaneously emerge from the algorithmic nature of evolution. *Proceedings of the National Academy of Sciences*, 119(11):e2113883119.

Kargar, B. H., Miras, K., and Eiben, A. (2021). The effect of selecting for different behavioral traits on the evolved gaits of modular robots. In *ALIFE 2021: The 2021 Conference on Artificial Life*. MIT Press.

Lan, G., De Carlo, M., van Diggelen, F., Tomczak, J. M., Roijers, D. M., and Eiben, A. E. (2021). Learning directed locomotion in modular robots with evolvable morphologies. *Applied Soft Computing*, 111:107688.

Luo, J., Stuurman, A. C., Tomczak, J. M., Ellers, J., and Eiben, A. E. (2022). The effects of learning in morphologically evolving robot systems. *Frontiers in Robotics and AI*, 9:797393.

Miras, K., De Carlo, M., Akhatou, S., and Eiben, A. (2020a). Evolving-controllers versus learning-controllers for morphologically evolvable robots. In *Applications of Evolutionary Computation: 23rd European Conference, EvoApplications 2020, Held as Part of EvoStar 2020, Seville, Spain, April 15–17, 2020, Proceedings 23*, pages 86–99. Springer.

Miras, K., Ferrante, E., and Eiben, A. E. (2020b). Environmental influences on evolvable robots. *PloS one*, 15(5):e0233848.

Miras, K., Haasdijk, E., Glette, K., and Eiben, A. E. (2018). Search space analysis of evolvable robot morphologies. In *Applications of Evolutionary Computation: 21st International Conference, EvoApplications 2018, Parma, Italy, April 4-6, 2018, Proceedings 21*, pages 703–718. Springer.

Møller, A. P. and Thornhill, R. (1998). Bilateral symmetry and sexual selection: a meta-analysis. *The American Naturalist*, 151(2):174–192.

Stanley, K. O., D'Ambrosio, D. B., and Gauci, J. (2009). A hypercube-based encoding for evolving large-scale neural networks. *Artificial life*, 15(2):185–212.

Toxvaerd, S. (2021). The emergence of the bilateral symmetry in animals: A review and a new hypothesis. *Symmetry*, 13(2):261.

Weisstein, E. W. (2003). Fermat points. *https://mathworld.wolfram.com/FermatPoints.html*.

APPENDIX

A Hyperparameter Selection Analysis

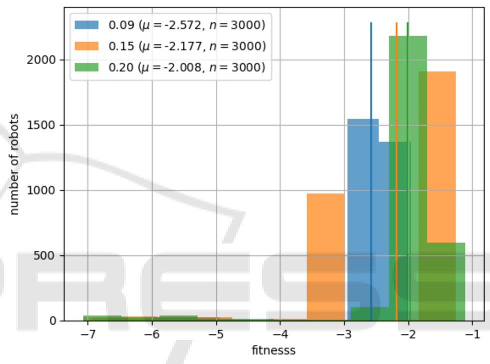

(a) Fitness distributions for different values of body mutation rates (p_{brain}).

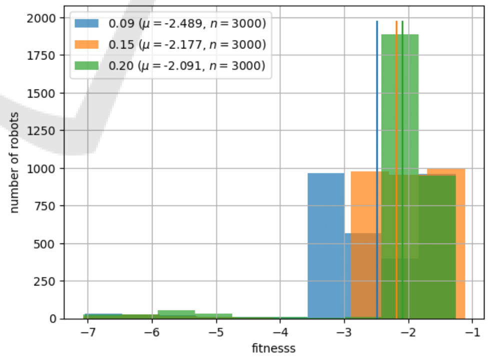

(b) Fitness distributions for different values of brain mutation rates (p_{brain}).

Figure 7: Comparing distributions of robots fitnesses of last generations over 30 experiments, while controlling, with grid search, for k and vision capability, given different values of mutation rates. $n = \mu * 30$.

While for the tournament size parameter k we saw some clear improvement in convergence using a higher value of 6 instead of 3, for the overall mutation rates of the "brain" and "body" genotypes we

SCITEPRESS SCIENCE AND TECHNOLOGY PUBLICATIONS

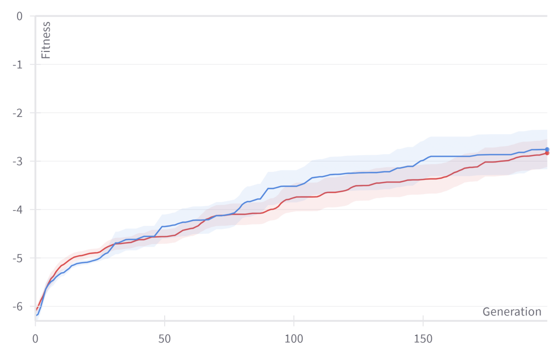

(a) Fitness results for condition T_1.

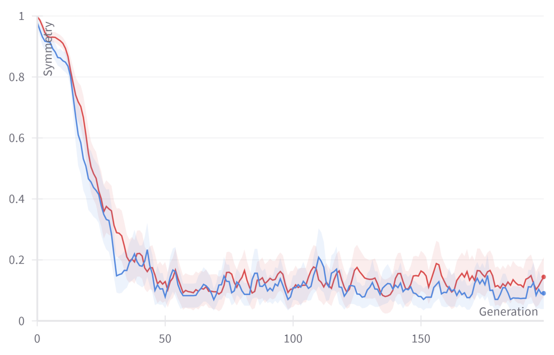

(b) Symmetry results for condition T_1

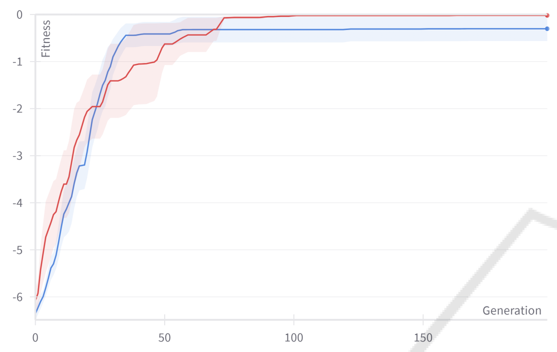

(c) Fitness results for condition T_2.

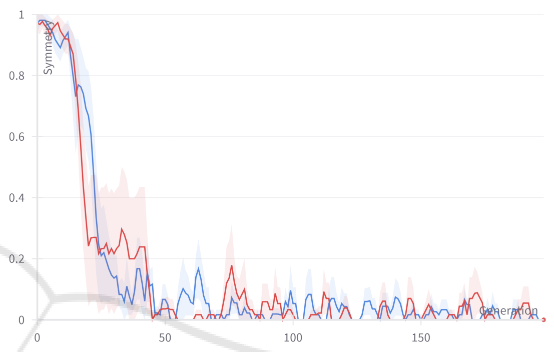

(d) Symmetry results for condition T_2

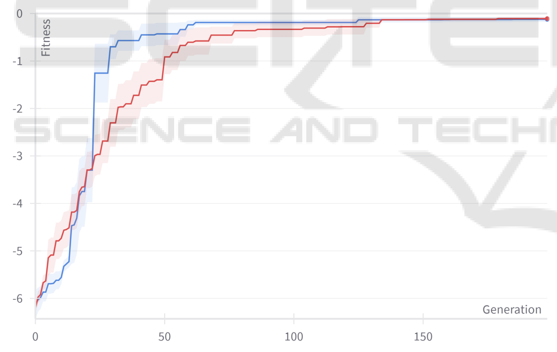

(e) Fitness results for condition T_3.

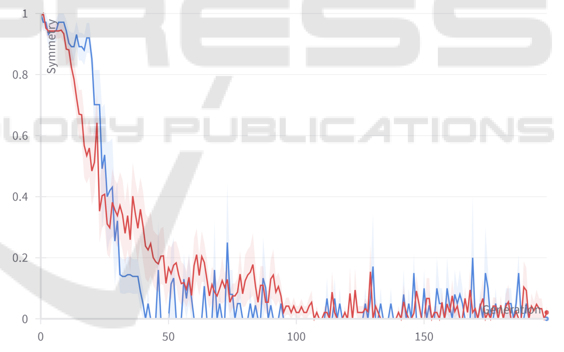

(f) Symmetry results for condition T_3

SCITEPRESS
SCIENCE AND TECHNOLOGY PUBLICATIONS

Figure 8: Mean of (max fitnesses per generations, left) and mean of (max symmetries per generations, right) over all runs for robots with steering behavior (blue) and without (red). The x-axis is the generation index and the y-axis is the fitness according to Equation 1 (left) or 3D symmetry according to Equation 4 (right). The shadows represent standard error.

didn't have conclusive results that would make us lean more towards a singular option. Because of this, for both genotypes, we chose the median of the values experimented during grid search. In Figure 7a and 7b we compare the distributions via histograms of the finesses attained in the hyperparameter selection task (targeted locomotion with the target at $(5,5)$). The analysis indicates that variations in this parameter do not significantly lead to better performances, thus motivating our decision.

B Terminating Simulations Early

With the aim of saving computation time, we experimented with prematurely stopping simulations, specifically targeting those where the robots failed to make sufficient progress towards the target beyond a certain threshold. This was motivated by the fact that we noticed how, especially in the first 40 generations, many robots weren't moving towards the correct direction or weren't moving at all. Thus, it may be useful to use the first few seconds of the robot's life as a heuristic to terminate its simulation earlier. This was achieved by defining a minimum velocity v_{min} and calculating the distance traveled towards the target at time t as:

$$s_t = d_o + f_t \tag{7}$$

Where d_o is the Euclidean distance between the origin (where the robot is generated) and the target, and f_t, which is negative, is the value of the fitness function at time t. Finally, s_t has to satisfy the following condition to avoid the termination of the simulation:

$$s_t \geq v_{min} \cdot t \cdot \sqrt{i_{gen}} \tag{8}$$

where i_{gen} is the generation index that goes between 0 and G_{max}. We multiply by $\sqrt{i_{gen}}$ to increase the value for higher generations as we assume that the robots are slowly performing better and we can expect higher standards of performance.

We empirically observed our computation time for 100 generations of 100 individuals being decreased by a factor of ≈ 3 as many simulations were killed especially in the first few generations. This reduction is particularly impactful, given that a single run of this type originally took ≈ 25 minutes. However, the mean fitness appeared to be marginally decreased by ≈ 0.2. Since computation efficiency was not the main focus of the research, we decided to abandon this method for the time being. Nevertheless, this approach could be developed further in future research for any task, and an improved strategy we suggest would be to adjust the threshold for the minimum speed based on the current average performance and the standard deviation within the population.

C Mean of Maximum Results per Generation

Figure 8 shows the relevant figures of the means of (max fitnesses per generations, left) and means of (max symmetries per generations, right) over all runs for robots with steering behaviour and without.

SCIENCE AND TECHNOLOGY PUBLICATIONS